Modeling Ultrasonic Wave Propagation in Prismatic Li-ion Battery Cells

SHENGYUAN ZHANG, PENG ZUO and ZHENG FAN

ABSTRACT

Accurate in-situ monitoring of key states in prismatic Li-ion battery cells, such as temperature, state of charge (SoC), and state of health (SoH), is critical for ensuring the safety and performance of electric transportation. Since these states are closely linked to the cells' internal mechanical properties, ultrasonic non-destructive testing (NDT) has emerged as a promising diagnostic approach. However, practical implementation remains challenging due to the complex nature of ultrasonic wave propagation within the cells' internal structure, which comprises stacked layers of porous electrodes and separators. While analytical methods like the transfer matrix method and Biot theory are widely used to model wave propagation in layered and porous media, they fall short in capturing the behavior of porous layers with heterogeneous solid frames. To address this, the present study develops finite-difference time-domain (FDTD) models that account for both inter-layer wave interactions and micro-scale fluid-solid coupling within the porous layers, enabling simulation of wave propagation through the thickness and along the plane of the cell layers. The simulation results are analyzed and compared with experimental data, and the resulting insights provide a deeper understanding of ultrasonic wave behavior in battery cells, laying a solid foundation for advancing ultrasonic-based battery state monitoring.

INTRODUCTION

Vehicles and aircraft powered by prismatic Li-ion battery cells have become a key component of modern transportation. Accurate monitoring of critical battery states—such as temperature, state of charge (SoC), and state of health (SoH)—is essential for optimizing performance and ensuring safety [1–3]. Since these states are intrinsically linked to the mechanical properties of the cell, ultrasonic non-destructive testing (NDT)—which

Shengyuan Zhang, PhD candidate, Department of Mechanical and Aerospace Engineering, Nanyang Technological University, Singapore
Peng Zuo, Scientist, Advanced Remanufacturing and Technology Centre (ARTC), Agency for Science, Technology and Research (A*STAR), Singapore
Zheng Fan, Associate Professor, Department of Mechanical and Aerospace Engineering, Nanyang Tech- nological University, Singapore. Email: zfan@ntu.edu.sg

provides rapid, non-invasive assessment of internal mechanical characteristics via penetrative ultrasonic waves—has emerged as a promising approach for battery state monitoring [4].

Although many experimental studies have reported strong correlations between ultrasonic features and battery states, a rigorous theoretical framework is still lacking. In particular, the specific mechanical properties responsible for the observed variations in ultrasonic signals remain unclear. Without theoretical validation, the repeatability of these empirical correlations remains uncertain, and their adaptability across different cell types, wave modes, and measurement conditions is significantly limited.

For example, conflicting findings have been reported in the literature. While several studies have investigated SoC estimation based on the travel time of ultrasonic waves transmitted through cell layers [5–8], others have found that travel time is largely insensitive to SoC [9, 10]. Similarly, the amplitude of both through-thickness transmitted waves [7, 11] and guided waves propagating along the layers [12–15] has shown inconsistent correlations with SoC across different studies. Moreover, puzzling amplitude variations have been observed during cycling, including the disappearance of linear trends after 60 cycles and contradictory behaviors across cells with similar chemistries but different capacities [16]. These discrepancies underscore the current limitations in the repeatability, robustness, and transferability of ultrasonic-based state estimation techniques, highlighting the urgent need for a theoretical framework that can account for and explain these observations.

The lack of a theoretical framework arises from the challenge of accurately describing ultrasonic wave propagation within the complex layered structure of battery cells, which includes electrolyte-saturated porous electrodes and separator layers. Consequently, conventional analytical methods, such as the transfer matrix method commonly used for modeling wave propagation in layered media [17], are not directly applicable. Moreover, the solid matrix of the electrodes is heterogeneous, consisting of active material particles bound by conductive binders, which violates the homogeneity assumption underlying the Biot theory for wave propagation in porous media [18].

In related fields such as seismology and medical ultrasound, numerical models that explicitly construct porous microstructures and incorporate fluid-solid interactions have been developed to simulate wave propagation in complex porous materials, such as rocks [19] and cancellous bone [20,21]. Building on this approach, the authors' previous work introduced a quasi-1D finite element model (FEM) for battery electrodes that inherently accounts for their heterogeneous solid frame and accurately simulates ultrasonic wave velocities [22].

However, accurately modeling wave propagation in both the through-thickness and in-plane directions of cell layers also necessitates modeling inter-layer interactions. In the in-plane direction, wave velocity emerges from the mechanical coupling between adjacent layers. In the through-thickness direction, multiple reflections at layer interfaces influence both the phase velocity and the transmission/reflection coefficients. Additionally, mode conversions between P-waves and Biot slow waves can occur at these interfaces, further affecting wave transmission behavior. To capture both the porous microstructure and the layered macrostructure within a unified framework, a large-scale numerical model is required. The finite-difference time-domain (FDTD) method is well-suited for this purpose due to its superior computational efficiency compared to FEM.

Therefore, this study aims to develop FDTD models to simulate ultrasonic wave propagation in both the through-thickness and in-plane directions of battery cell layers. The subsequent sections present the model formulation and simulation results, including signal, wavefield, and feature analyses, parametric studies, and comparisons with experimental data. Finally, key insights derived from the simulations are discussed to deepen the understanding of wave behavior within the layered battery structure.

METHOD

Without loss of generality, this study focuses on a commercial 50 Ah $LiFePO_4$ prismatic cell (EVE LF50K). The cell layered structure comprises five types of layers: anode, anode current collector (CC), cathode, cathode CC, and separator. Copper and aluminum foils are CCs for the anode and cathode, respectively. Active material particles, graphite for the anode and $LiFePO_4$ for the cathode, are coated on both sides of the CCs using conductive binders as the frame material, forming the anode and cathode layers. These layers are stacked alternately with separators in between. The separators, made of porous polypropylene (PP), provide pathways for lithium ion transport while preventing internal short circuits. Liquid electrolytes fill the pores of the anode, cathode, and separator layers, enabling lithium-ion transport throughout the cell.

The FDTD models of the prismatic cell were developed using SimSonic, a free software package created by Prof. Bossy [20]. SimSonic employs the velocity-stress formulation to describe wave dynamics in both fluid and solid media. In Cartesian coordinates, this formulation is expressed as:

$$\rho(\mathbf{x})\frac{\partial v_i}{\partial t}(\mathbf{x},t) = \sum_{j=1}^{d}\frac{\partial T_{ij}}{\partial x_j}(\mathbf{x},t) + f_i(\mathbf{x},t) \tag{1}$$

and

$$\frac{\partial T_{ij}}{\partial t}(\mathbf{x},t) = \sum_{j=1}^{d}\sum_{i=1}^{d} C_{ijkl}(\mathbf{x})\frac{\partial v_k}{\partial x_l}(\mathbf{x},t) + \theta_{ij}(\mathbf{x},t), \tag{2}$$

where d is the spatial dimension, $\mathbf{x}$ and t are the spatial and temporal variables, $\rho(\mathbf{x})$ is the local mass density, and $C_{ijkl}(\mathbf{x})$ are the components of the fourth-order stiffness tensor. The particle velocity components are denoted by $v_i(\mathbf{x},t)$, and the stress tensor components by $T_{ij}(\mathbf{x},t)$. External body forces are represented by f_i, while θ_{ij} denotes components of strain rate sources.

The spatial dimension must be three (that is, $d = 3$) because the interconnected nature of both fluids and solids in porous media requires a fully 3D model.

Geometry and material heterogeneities are modeled directly by defining spatially varying material property maps, $\rho(\mathbf{x})$ and $C_{ijkl}(\mathbf{x})$. For example, in the electrode layers, active material particles, conductive binders, and electrolytes are individually represented by assigning their respective properties to designated spatial regions. Since each component material is isotropic, the stiffness tensor $C_{ijkl}(\mathbf{x})$ is expressed using only two independent parameters: the bulk modulus K and the shear modulus μ. The fluid phase (electrolyte) is incorporated into this framework by assigning it a zero shear modulus. The continuity of pressure and normal velocity at fluid-solid interfaces is inherently

captured through these material property assignments, enabling accurate modeling of microscale fluid-solid interactions and wave behavior in the porous layers.

The properties of all component materials are obtained from the literature and are summarized in Table I.

TABLE I. Material properties of the prismatic cell.

Material	ρ [kg/m^3]	K [GPa]	μ [GPa]
Al	2700	84	29
Cathode binder [23]	1960	1.78	0.59
$LiFePO_4$ [24]	3520	94.3	44.3
PP	900	1.38	0.92
Graphite [25]	2260	29.3	12.3
Anode binder [26]	1640	0.56	0.19
Cu	8960	137	47
Electrolyte	1270 [9]	2.49 (Measured)	0

To solve for the unknown fields $v_i(\mathbf{x}, t)$ and $T_{ij}(\mathbf{x}, t)$, central difference approximations are applied to the spatial and temporal partial derivatives in Equations (1) and (2). The simulation domain is discretized on regular grids with a temporal step Δt and a spatial step Δx. The spatial step must be small enough to capture the microstructural details and ensure smooth field representations, while the temporal step is chosen according to the Courant–Friedrichs–Lewy (CFL) condition to ensure the numerical stability and accuracy of wave propagation.

In this study, spatial step sizes no larger than 2 μm were selected considering that both the layer thickness and the size of active particles are on the scale of 10 μm. By referring to the layer thicknesses and material volume fractions within each layer, roughly estimated from the material weight fractions given by the manufacturer and the number of layers obtained from X-ray CT imaging, an approximated cell geometry can be constructed with a regular grid at the selected step size. In the electrode layers, active material particles ($LiFePO_4$ and graphite) are modeled as cubes, while conductive binders are represented as cuboids connecting the particles. The solid phase of the separator (PP) is modeled as a regular frame structure. Figure 2 shows a representative unit of the layered structure in the model at different step sizes. The unit is symmetric across all six faces relative to adjacent units, so the Cu and Al layers are visualized with half thickness. The geometric parameters of the individual layers in the model are listed in Tables II and III. The modeled geometry yields material weight fractions that closely match the actual values, as shown in Table IV.

Since the separator is not bonded to the electrodes, additional interfacial layers with unit-thickness are introduced between their solid phases to simulate weak interfaces [27–30]. These layers account for frictional forces from the internal pressure of the cell, ensuring stress continuity through the thickness. However, sliding may occur at the interface, resulting in in-plane displacement discontinuities. Such discontinuities influence not only the ultrasonic velocity along the layers but also the through-thickness transmission of P-waves due to the inhomogeneous nature of the medium. To capture

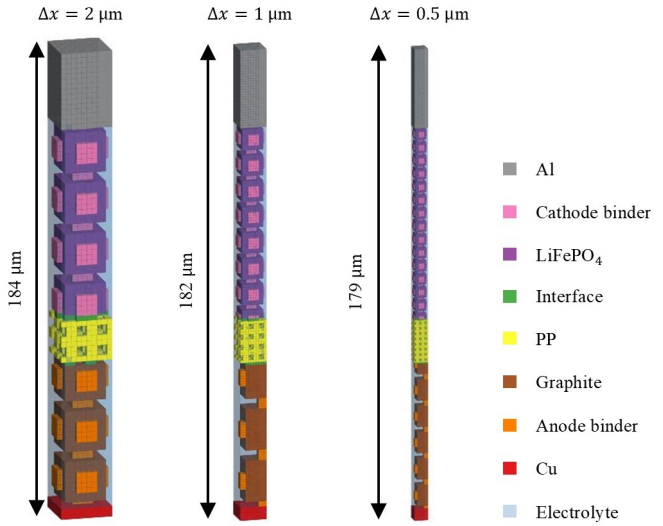

Figure 1. Representative units of acoustic simulation models with spatial step sizes of 2 μm, 1 μm, and 0.5 μm.

TABLE II. Geometric parameters of the layers in the simulation model for the prismatic cell.

Layer	Number	Thickness [μm]		
	(X-ray CT)	$\Delta x = 2\mu$m	$\Delta x = 1\mu$m	$\Delta x = 0.5\mu$m
Cathode CC	76	60	60	60
Cathode	152	74	74	72.5
Separator	160	16	16	16
Anode	160	56	55	55
Anode CC	80	8	10	9

this behavior, the interfacial layers are assigned the properties of PP, except for the shear modulus, which is set to a very small but non-zero value—allowing shear stress continuity while permitting relative in-plane motion.

As illustrated in Fig. 2, for simulating through-thickness transmission, the representative unit and its mirror reflection along the thickness direction are combined to form a repetitive unit, which is then extended through the cell thickness. A plane wave source is applied to the top surface in the thickness direction, and transmitted waves are recorded at the bottom surface. Owing to the symmetry in both geometry and wavefields, symmetric boundary conditions are applied on the four lateral surfaces, resulting in a quasi-1D model. Similarly, a model for in-plane transmission is constructed using the same approach, also shown in Fig. 2.

RESULTS

TABLE III. Material volume fraction in the individual layers of the simulation model for the prismatic cell.

Layer	Material	Volume fraction		
		$\Delta x = 2\mu$m	$\Delta x = 1\mu$m	$\Delta x = 0.5\mu$m
Cathode CC	Al	100%	100%	100%
Cathode	$LiFePO_4$	51.9%	51.0%	51.2%
	Binder	9.9%	9.5%	9.6%
	Electrolyte	38.2%	39.5%	39.2%
Separator	PP	50%	50%	50%
	Electrolyte	50%	50%	50%
Anode	Graphite	52.6%	52.4%	51.2%
	Binder	9.7%	5.6%	5.4%
	Electrolyte	37.7%	42.0%	43.4%
Anode CC	Cu	100%	100%	100%

TABLE IV. Material weight fraction of the prismatic cell.

Material	Actual weight	Modeled weight		
		$\Delta x = 2\mu$m	$\Delta x = 1\mu$m	$\Delta x = 0.5\mu$m
Al	19%	20%	19%	20%
LFP	33%	33%	32%	32%
PP	2%	2%	2%	2%
Graphite	18%	17%	16%	16%
Cu	11%	9%	11%	10%
Electrolyte	17%	18%	19%	19%

The wave propagation behavior within individual porous layers—the anode, cathode, and separator—is first investigated. Each type of layer is modeled as a homogeneous bulk medium. Quasi-1D models are constructed by leveraging symmetry in directions perpendicular to wave propagation. Along the propagation direction, free boundary conditions are applied at both ends. A narrowband velocity excitation is uniformly applied to one end, and the transmitted waves are recorded at the opposite end as the surface-integrated velocity. The model length is set to 10 mm to ensure the separation between P-waves and Biot slow waves and to avoid overlap between the first and second arrivals of P-waves caused by reflections at the two ends. Figure 3(a) shows a representative section of the quasi-1D anode model with a 2 μm spatial step size.

The P-wave velocities are derived from the phase shift between the excitation and reception signals, yielding values of 1538.5 m/s in the cathode, 1427.4 m/s in the separator, and 1351.7 m/s in the anode. Referring to the total thicknesses of the respective layer types in Table II and estimating travel time by dividing these by their corresponding velocities gives a through-thickness travel time of 16.8 μs.

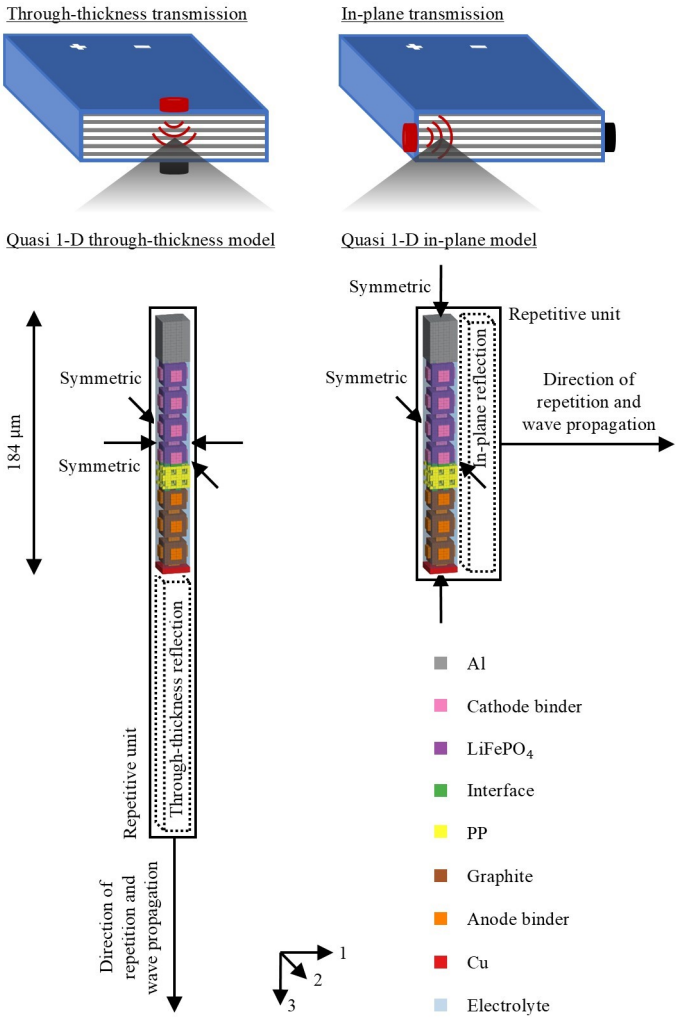

Figure 2. Acoustic simulation models for through-thickness transmission and in-plane transmission, using the representative unit with a 2 μm spatial step size.

In porous media, an additional type of longitudinal wave—known as the Biot slow wave—propagates more slowly than P-waves. The models successfully reproduce this phenomenon. Figure 3(b) shows the wavefield in a section located 1100–1300 μm from the source in the quasi-1D anode model at 7 μs, when the Biot slow waves at 1 MHz are passing through. At this time instant, the P-waves and Biot slow waves are clearly separated, as illustrated by the full wavefield in Figure 3(b). The fluid and solid domains are observed to oscillate in counter-phase, which is consistent with Biot theory.

It was found that wave velocity is not affected by particle size. Simulations conducted with smaller spatial step sizes and reduced particle sizes exhibited similar wave behavior. This suggests that wave propagation is primarily determined by macroscopic parameters, such as material volume fractions.

For wave propagation through the cell thickness (along the 3-direction), both amplitude and travel time are influenced by multiple reflections at the layer interfaces. Figure 4(a) presents an experimental signal measured in pulse-echo mode using two broadband

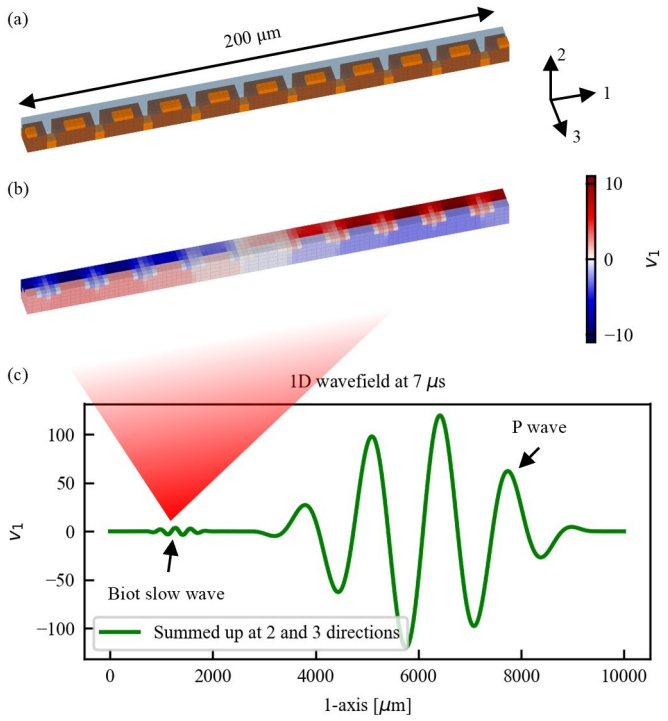

Figure 3. (a) A section of the quasi-1D anode model. (b) Example wavefield illustrating Biot slow waves at 1 MHz. (c) 1D wavefield of the full anode model at 7 μs.

commercial probes (Olympus V106). The first arrival occurs at approximately 18 μs. Following this, an additional pulse with lower amplitude is observed, which is attributed to strong reflections at the triple-separator gaps inside the cell. Notably, although the excitation signal is centered at 1 MHz, the received signal is centered around 600 kHz, indicating that higher frequencies experience greater attenuation and lower transmission.

The modeled through-thickness transmission signals at different spatial step sizes are also shown in the figure. With a 2 μm step size, the travel time is 20.5 μs—substantially longer than the estimated 16.8 μs obtained without accounting for the reflections at layer interfaces. This highlights the importance of explicitly modeling the layered structure to accurately capture the through-thickness travel time.

However, the modeled travel time remains longer than the experimental value, likely due to geometric inaccuracies and the imprecise modeling of weak interfaces. This discrepancy decreases with smaller spatial step sizes, as shown in Table V, possibly due to reduced binder volume fractions (see Table II) and thinner weak interfacial layers in the finer models.

Additional simulations also indicate that the interfacial stiffness at weak interfaces influences the travel time. Thus, part of the discrepancy may stem from inaccuracies in assigning this parameter.

Figure 4(b) presents the modeled through-thickness transmission signals using a 2 μm spatial step size at various narrowband excitation frequencies. Across the 200 kHz to 1 MHz range, the arrival time remains constant, indicating no dispersion within this frequency range.

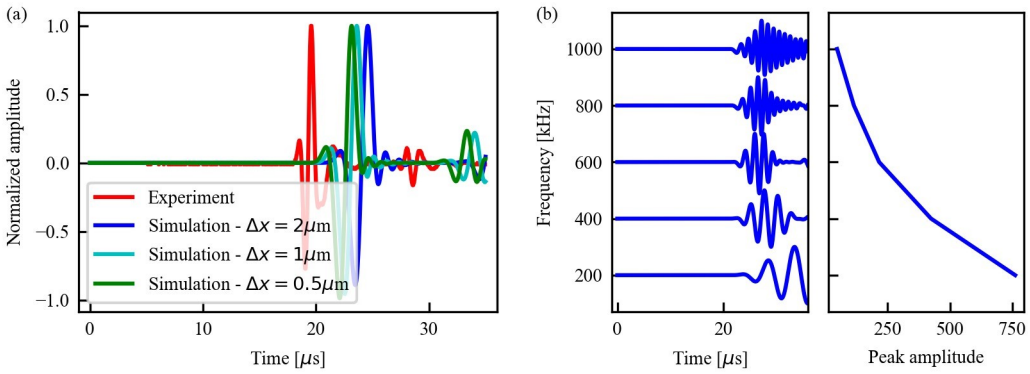

Figure 4. (a) Experimental and modeled through-thickness transmission signals under broadband excitation; later pulses result from internal triple-separator gap reflections. (b) Modeled through-thickness transmission signals using 2 μm step size at various narrowband excitation frequencies and their corresponding peak amplitudes.

TABLE V. Through-thickness travel times by experiment and simulation.

	Experiment	Simulation		
		$\Delta x = 2\mu$m	$\Delta x = 1\mu$m	$\Delta x = 0.5\mu$m
Travel time [μs]	18.0	20.5	19.8	19.4

The simulation also reveals that higher-frequency signals exhibit lower peak amplitudes. This attenuation is primarily due to reflections at the numerous layer interfaces and mode conversion from P-waves to Biot slow waves.

For the simulation of in-plane transmission, the tangential displacement (along the 1- and 2-directions) continuity across the weak interface was found to be a key parameter. However, this parameter depends on the internal pressure and is not measurable or known in advance. Therefore, we present a parametric study here by the model with a 2 μm spatial step size. The displacement discontinuity is tuned by the shear modulus of the weak interface. The shear modulus cannot be too small; otherwise, decoupling occurs between the waves at different layers, as shown in Figure 5(a). With an appropriate shear modulus, the waves across different layers are coupled and propagate as a single wave. These waves reflect off the right free boundary without additional phase shift. The wave velocity can be calculated based on the phase shift between the signals received at the two ends of the model, as illustrated in Figure 5(b). By varying the shear modulus within a suitable range, the relationship between in-plane velocity and shear modulus is established, as shown in Figure 5(c). We observe that the wave velocity increases with shear modulus but gradually converges.

In the experiment, the in-plane velocity was measured using two PZT disks with a resonant frequency of 200 kHz in a pitch-catch mode. The measured wave velocity was approximately 2500 m/s, which is clearly smaller than the simulated values. From the simulation, we know that reducing the simulated velocity to match the experiment

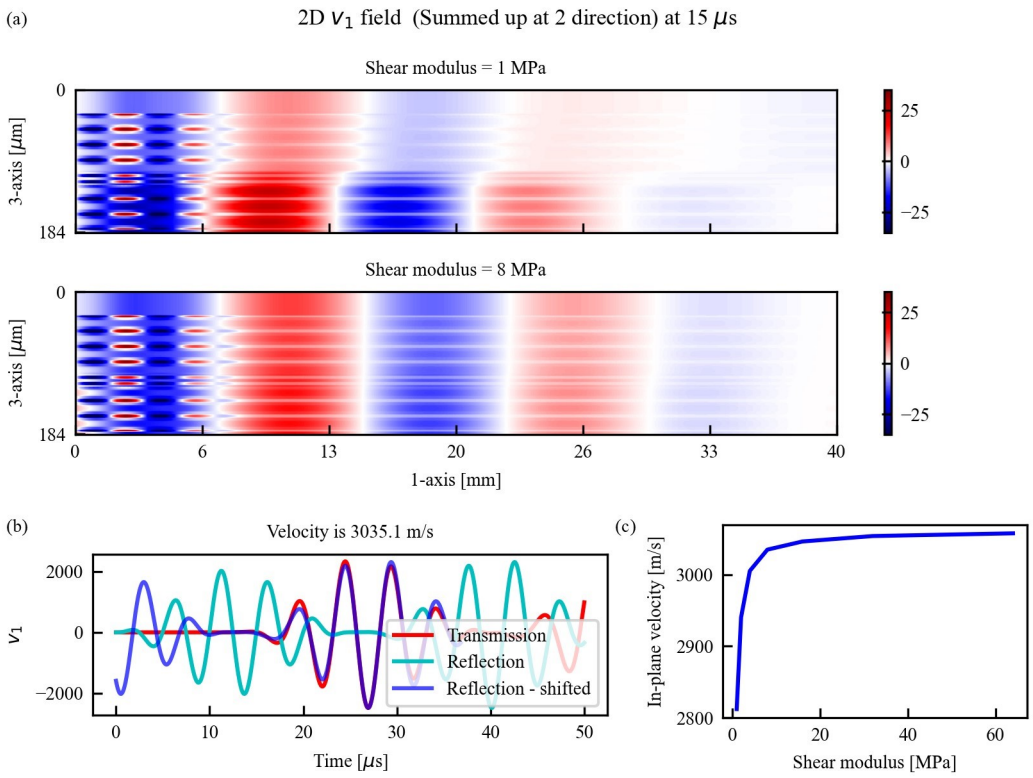

Figure 5. (a) 2D wavefield of in-plane transmission at 200 kHz excitation; the short-wavelength waves are Biot slow waves, while the faster waves are P-waves, which exhibit decoupling between layers when the shear modulus of the weak interfaces between electrodes and the separator is 1 MPa. (b) Signals recorded at the right end (Transmission) and the left end (Reflection) under 200 kHz excitation and a weak interface shear modulus of 8 MPa, with an illustration of wave velocity calculation based on the phase shift between the two signals. (c) In-plane wave propagation velocities at different shear moduli.

would lead to layer decoupling, which is unrealistic. This discrepancy must therefore be accepted and is also likely due to geometric inaccuracies in the model.

CONCLUSION

In this study, full-scale FDTD models were successfully developed to simulate both through-thickness and in-plane wave propagation within the layered structure of a Li-ion cell. The Biot slow waves within the porous layers were accurately captured, exhibiting lower velocities than P-waves and counter-phase motion between the fluid and solid phases, consistent with Biot theory. The results demonstrate that multiple reflections within the layered structure significantly affect the through-thickness travel time. Additionally, no dispersion was observed within the 200 kHz to 1 MHz frequency range. Strong reflections at triple-separator gaps, as observed in the experiments, were also reproduced in the simulation. Furthermore, the transmission amplitude was found to be

frequency-dependent, with higher frequencies showing reduced amplitudes due to multiple reflections and mode conversion between P-waves and Biot slow waves at layer interfaces. Although other attenuation mechanisms were not modeled, the observed frequency-dependent amplitude trend aligns well with experimental results.

For in-plane transmission, the simulation reveals a strong dependence of wave velocity on the tangential displacement continuity across the weak interfaces between electrodes and separators.

Nevertheless, discrepancies remain between simulation and experimental measurements, particularly in through-thickness travel time and in-plane velocity. These differences are likely due to geometric inaccuracies in the model, which are challenging to address given the limited geometric flexibility of the FDTD method. Future work should consider adopting more advanced modeling approaches to better capture the complex internal structure of the cell and enhance simulation accuracy.

ACKNOWLEDGMENT

We gratefully acknowledge support from MOE AcRF Tier 1, RG149/23 and A*STAR (Career Development Fund, project no. C222812020).

REFERENCES

1. Waag, W., C. Fleischer, and D. U. Sauer. 2014. "Critical review of the methods for monitoring of lithium-ion batteries in electric and hybrid vehicles," *Journal of Power Sources*, 258:321–339.
2. Ma, S., M. Jiang, P. Tao, C. Song, J. Wu, J. Wang, T. Deng, and W. Shang. 2018. "Temperature effect and thermal impact in lithium-ion batteries: A review," *Progress in Natural Science: Materials International*, 28(6):653–666.
3. Guo, X., Y. Yang, C. Shi, M. Xu, Y. Liu, and D. Zou. 2025. "Monitoring and control of internal temperature in power batteries: A comprehensive review," *Energy Storage Materials*:104051.
4. Williams, D., R. Copley, P. Bugryniec, R. Dwyer-Joyce, and S. Brown. 2024. "A review of ultrasonic monitoring: Assessing current approaches to Li-ion battery monitoring and their relevance to thermal runaway," *Journal of Power Sources*, 590:233777.
5. Davies, G., K. W. Knehr, B. Van Tassell, T. Hodson, S. Biswas, A. G. Hsieh, and D. A. Steingart. 2017. "State of charge and state of health estimation using electrochemical acoustic time of flight analysis," *Journal of The Electrochemical Society*, 164(12):A2746.
6. Kim, J.-Y., J.-H. Jo, and J.-W. Byeon. 2020. "Ultrasonic monitoring performance degradation of lithium ion battery," *Microelectronics Reliability*, 114:113859.
7. Sun, H., N. Muralidharan, R. Amin, V. Rathod, P. Ramuhalli, and I. Belharouak. 2022. "Ultrasonic nondestructive diagnosis of lithium-ion batteries with multiple frequencies," *Journal of Power Sources*, 549:232091.
8. Borujerdi, A. S., C. Jin, and J. Zhu. 2024. "Ultrasonic monitoring of lithium-ion batteries with in-situ self-temperature correction," *Journal of Power Sources*, 597:234103.
9. Gold, L., T. Bach, W. Virsik, A. Schmitt, J. Müller, T. E. Staab, and G. Sextl. 2017. "Probing lithium-ion batteries' state-of-charge using ultrasonic transmission–Concept and laboratory testing," *Journal of Power Sources*, 343:536–544.

10. Han, J., C. Yuan, J. Long, J. Wu, and M. Lin. 2024. "An Ultrasonic Reflected Wave-Based Method for Estimating State of Charge of Hard-Shell Lithium-Ion Batteries," *IEEE Transactions on Instrumentation and Measurement*.
11. Feiler, S., L. Gold, S. Hartmann, and G. A. Giffin. 2024. "Investigation of Acoustic Attenuation and Resonances in Lithium-Ion Batteries Using Ultrasound Spectroscopy," *Batteries & Supercaps*, 7(10):e202400212.
12. Ladpli, P., F. Kopsaftopoulos, and F.-K. Chang. 2018. "Estimating state of charge and health of lithium-ion batteries with guided waves using built-in piezoelectric sensors/actuators," *Journal of Power Sources*, 384:342–354.
13. Koller, M., G. Glanz, R. Jaber, and A. Bergmann. 2023. "Ultrasonic Battery Management System for Lamb wave mode tracking on Lithium-ion pouch cells," *Journal of Energy Storage*, 74:109347.
14. Liu, B., W. Tong, Y. Cao, and J. Li. 2024. "SOC estimation method based on the ultrasonic guided waves considering the significant effect of charge/discharge rate," *Journal of Energy Storage*, 87:111434.
15. Sampath, S., X. Yin, Z. W. Tham, Y. F. Chen, and L. Zhang. 2024. "Real-time and non-contact estimation of state of charge for lithium-ion battery using laser ultrasonics," *Journal of Power Sources*, 605:234544.
16. Wu, Y., Y. Wang, W. K. Yung, and M. Pecht. 2019. "Ultrasonic health monitoring of lithium-ion batteries," *Electronics*, 8(7):751.
17. Lowe, M. J. 1995. "Matrix techniques for modeling ultrasonic waves in multilayered media," *IEEE transactions on ultrasonics, ferroelectrics, and frequency control*, 42(4):525–542.
18. Carcione, J. M. J. M. 2007. *Wave fields in real media: Wave propagation in anisotropic, anelastic, porous and electromagnetic media*, Elsevier.
19. van Vossen, R., J. O. Robertsson, and C. H. Chapman. 2002. "Finite-difference modeling of wave propagation in a fluid-solid configuration," *Geophysics*, 67(2):618–624.
20. Bossy, E. and Q. Grimal. 2011. "Numerical methods for ultrasonic bone characterization," *Bone quantitative ultrasound*:181–228.
21. Vafaeian, B., M. El-Rich, T. El-Bialy, and S. Adeeb. 2014. "The finite element method for micro-scale modeling of ultrasound propagation in cancellous bone," *Ultrasonics*, 54(6):1663–1676.
22. Zhang, S., P. Zuo, X. Yin, and Z. Fan. 2024. "Exploring the correlation between ultrasound time of flight and the state of health of LiFePO4 prismatic cells," *Journal of Energy Storage*, 83:110715.
23. Grillet, A. M., T. Humplik, E. K. Stirrup, S. A. Roberts, D. A. Barringer, C. M. Snyder, M. R. Janvrin, and C. A. Apblett. 2016. "Conductivity degradation of polyvinylidene fluoride composite binder during cycling: Measurements and simulations for lithium-ion batteries," *Journal of The Electrochemical Society*, 163(9):A1859.
24. Maxisch, T. and G. Ceder. 2006. "Elastic properties of olivine Li x FePO 4 from first principles," *Physical Review B*, 73(17):174112.
25. Qi, Y., H. Guo, L. G. Hector, and A. Timmons. 2010. "Threefold increase in the Young's modulus of graphite negative electrode during lithium intercalation," *Journal of The Electrochemical Society*, 157(5):A558.
26. Hu, H., B. Tao, Y. He, and S. Zhou. 2019. "Effect of conductive carbon black on mechanical properties of aqueous polymer binders for secondary battery electrode," *Polymers*, 11(9):1500.
27. Nagy, P. B. 1992. "Ultrasonic classification of imperfect interfaces," *Journal of Nondestructive evaluation*, 11:127–139.
28. Baltazar, A., L. Wang, B. Xie, and S. Rokhlin. 2003. "Inverse ultrasonic determination of

imperfect interfaces and bulk properties of a layer between two solids," *The Journal of the Acoustical Society of America*, 114(3):1424–1434.

29. Lanza di Scalea, F., P. Rizzo, and A. Marzani. 2004. "Propagation of ultrasonic guided waves in lap-shear adhesive joints: case of incident A 0 Lamb wave," *The Journal of the Acoustical Society of America*, 115(1):146–156.
30. Hosten, B. and M. Castaings. 2005. "Finite elements methods for modeling the guided waves propagation in structures with weak interfaces," *The Journal of the Acoustical Society of America*, 117(3):1108–1113.